Aerodynamic Behavior of Formula Student Open-Wheel Race Car Model with Regard to Head Restraint/Rear Wing Interaction

Ben Steinfurth Technische Universität Berlin

Steffen Feldhus FaSTTUBe Formula Student Team TU Berlin

Arne Berthold and Frank Haucke Technische Universität Berlin

Abstract

A realistic open-wheel race car model is investigated experimentally by means of surface flow visualization using UV active tufts, wall pressure as well as force measurements. The head restraint size is varied and crosswind conditions are reproduced inside a closed test section with a non-moving ground. An assessment of the aerodynamic components determines the contributions of front wing, rear wing and side wings with respect to the performance of the race car. Maximum downforce of the order of $c_L \approx -0.35$ (front wing only), $c_L \approx -1.4$ (front wing and rear wing combined) and $c_L \approx -1.5$ (complete aero package) are found at a neutral yaw angle. By means of flow visualization and image subtraction techniques, regions of highly turbulent flow on the rear wing are identified. They are shown to grow in size when the largest head restraint is installed. As a result, the pressure distribution for this configuration exhibits a consistent decrease in magnitude. In the case of the smaller investigated head restraints, only marginal deviations are detected. The disadvantage of the largest head restraint, however, becomes less pronounced at small yaw angles, reaching a maximum in downforce at $|\beta| \approx 6°$. Nonetheless, the application of a head restraint with a size exceeding a certain threshold is accompanied with a significant loss in downforce performance of the order of $\Delta c_L \approx 5.5\%$, as we are able to show in this article.

Introduction

The performance of a race car is determined by a number of contributing factors, such as engine power, suspension system, tire characteristics and human decision making. However, one of the most effective means in reducing lap times is the application of components which alter the aerodynamic properties of the vehicle. By utilizing rudder-type end plates, the lateral stability is increased [1,2], enabling better handling of the race car. Furthermore, inverted wings and diffusers generate a downforce (negative lift) more than two times the weight force of the car [3]. Thus, traction between tires and road is increased, allowing for a greater cornering speed. While every circuit boasts specific challenges with respect to downforce and drag, depending on the proportion of corners and straight sections, an increased downforce generally more than offsets the drag penalty induced by the aerodynamic package. The significance of this measure is illustrated by the finding that an increase in downforce by 1% yields a lap time reduction of 0.1 s around Silverstone Grand Prix Circuit [4].

Within the present experimental study, the aerodynamic package of an open-wheel Formula Student race car model is assessed. While doing so, the influence of head restraint size on the efficiency of the rear wing is investigated.

When designing aerodynamic components of a race car, the interaction of individual elements must be regarded. For instance, a front wing can exhibit optimal downforce characteristics when viewed separately but does not necessarily ensure an ideal, clean flow toward the body, engine intake and rear wing. Thus, the total downforce may be reduced or the drag is increased to an undesirable extent. A parametric steady-state computational study regarding the interfering effects of aerodynamic components of a Formula-1 car is conducted in [5]. It is found that the downforce can be increased by a factor of 2 when aerodynamic add-on devices, such as front and rear wing, a roof spoiler and wheel covers are applied. At the same time, a drag coefficient reduction by $\Delta c_D \approx 5\%$ is achieved. Another numerical investigation aiming at optimizing the body and undertray of a Formula SAE race car is presented in [6]. The downforce of the optimized undertray alone, consisting of three rear diffuser tunnels, is of the order of $c_L = -0.9$ while the total downforce of the race car is as great as $c_L = -2.4$ with a drag coefficient of $c_D \le 1.1$. The results are validated by experiments, however, determining a downforce performance that is smaller by $\Delta c_L = 6\%$. An experimental study of a 1:4 scale IndyCar model with non-rotating wheels and non-moving ground is in agreement with the

aforementioned investigation and shows that downforce is mainly determined by the underbody geometry as well as the front and rear wing [7].

Regarding the wings, the degree of fluid deflection majorly determines the wall pressure distribution, i. e., the force generated. An experimental study of a race car front wing shows that a flap deflection increased by $\Delta\alpha = 10°$ yields a downforce enhancement by $\Delta c_L \approx 40\%$ generated by the respective wing while the effect on aerodynamic drag is negligible [3]. A computational as well as experimental design process of a three-element rear wing of a Formula SAE race car is described in [8]. The angle of attack of the center element of this wing can be varied by the driver, enabling greater downforce during cornering maneuvers while smaller angles of attack are set at high speed sections, decreasing downforce as well as drag and thus, fuel consumption. A prototype is constructed and successfully track tested. A further study regarding smart flaps for race cars, representing airfoils with variable camber, shows that the lift/drag ratio can be increased by this measure [9]. A numerical study of the front and rear wing of a Formula Mazda race car under various angles of attack is documented in [10]. A critical angle of attack of $\alpha \approx 12°$ is identified with a marked drop in downforce due to distinct areas of flow separation beyond this threshold.

Furthermore, ground proximity of the front wing is assessed and singled out as a significant parameter. This can be explained by a more distinct suction side of the wing due to greater velocities of the bounded fluid. This mechanism, conventionally termed 'ground effect', is utilized by race car designers and has been object of numerous investigations, generally showing that the generated downforce is dependent on the normalized ground clearance h/c. A computational study [11] finds that the pressure magnitude on the suction side of a symmetric front wing increases by 18.6% from $h/c = 0.3$ to $h/c = 0.22$ with the downforce generated by the wing, then amounting to one third of the total downforce of the studied race car. An investigation of a highly cambered single-element wing shows that the downforce increases up to a ground clearance of $h/c = 0.1$ before flow separation occurs, causing a drop in downforce [12]. The ground effect is significantly marginalized in the wake of another flow body, i. e., during slipstream driving [13,14]. The effect, however, does not only apply to the front wing but also to the underbody of race cars, where the same observation regarding the correlation between ground clearance and downforce is made [15] with the aerodynamic load further increased by means of vortex generators in [16]. However, catastrophic failure can emerge from a combination of high speed, insufficient ground clearance and steep angles of attack as outlined in [17].

The present study investigates a Formula Student race car model (1:3 scale) that exhibits a relatively short distance between head restraint and rear wing cascade. Furthermore, no specific passive measures are taken to condition the flow downstream of the driver so that the rear wing inflow is generally determined by the geometries of helmet and head restraint. While the minimal size of the latter is limited by competition regulations due to safety issues, an enlargement of the device is not prohibited but may have negative implications on the downforce performance. The aim of this experimental study consists in the identification of a head restraint size that ensures the safety of the driver according to current regulations and does not negatively affect the aerodynamic properties of the race car model. In order to do so, wind tunnel tests are performed where the model is equipped with head restraints of different size. The induced wall pressure distributions on the three-element rear wing are assessed in multiple longitudinal sections and areas of separated flow are visualized by means of UV active tufts. Additionally, force measurements are conducted with the aid of a lever balance to gain insight regarding the influence of the studied head restraint/rear wing interaction on aerodynamic coefficients. While doing so, the yaw angle is varied within the range of $\beta = -21°, …, 21°$.

Experimental Setup

The experimental setup as well as the measurement procedure are outlined in the following before information regarding the applied experimental methods is provided.

Race Car Model

The investigated model, shown in Figure 1, represents a realistic open-wheel Monoposto race car and is derived from the current *FT17* model designed by the *FaSTTUBe - Formula Student Team TU Berlin*. Its aero package features a front wing, side wings and a rear wing of which the respective volumes are limited by competition regulations. Thus, the dimensions of the rear wing must not exceed the inner sides of the rear wheels and the head restraint and must not overlap the wheels in streamwise direction by more than 250 mm. The projected frontal area of the model is of the order of $A_x \approx 0.13$ m^2 and the base length is $L \approx 1012$ mm. Reynolds number independency regarding the downforce is achieved at $Re = \dfrac{U_\infty \cdot l_{wb}}{\nu} > 750{,}000$ with the wheelbase $l_{wb} = 0.53$ m considered the characteristic length. The presented results are obtained at a Reynolds number of $Re \approx 1{,}000{,}000$.

FIGURE 1 Top view of model; origin of coordinate system lies in symmetry plane at leading edge of rear wing; dimensioning in mm.

© SAE International
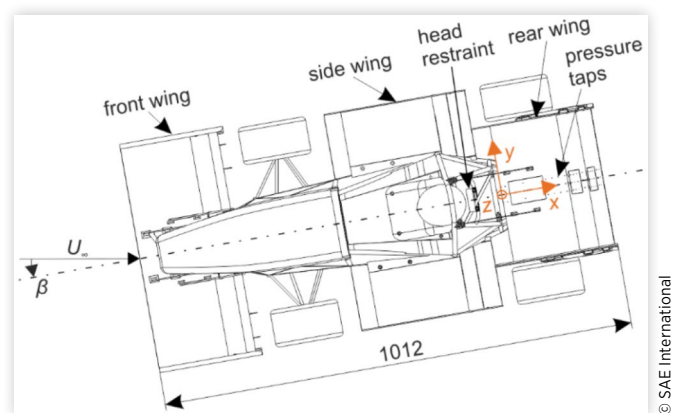
TABLE 1 Geometrical specifications of rear wing elements; angle of attack with reference to the horizontal.

Rear wing element	Chord length [mm]	Angle of attack [°]
Lower Wing (LW)	150.0	−5.2
Middle Wing (MW)	66.7	36.6
Upper Wing (UW)	66.7	60.8

© SAE International

TABLE 2 Investigated configurations with respect to head restraint size.

Configuration Label	Height of Head Restraint [mm]
HR0	none
HR1	50.0
HR2	66.5
HR3	93.0
HR4	113.3

© SAE International

FIGURE 2 Experimental setup inside the test section; reflex camera installed at positions 1 and 2 only during flow visualization; dimensioning in mm.

© SAE International

The rear wing consists of the three elements characterized in Table 1. For the present study, it features 40 pressure taps in streamwise direction inside the symmetry plane, see Figure 3. The pressure taps are connected to tubes, which are guided through the end plates, the engine compartment and the wind tunnel floor to the sensor and data acquisition system outside the wind tunnel.

Due to the high degree of complexity concerning the original vehicle, the 1:3 scale model exhibits minor simplifications. The wheels are non-rotating and the steering angle is fixed. Furthermore, the engine is removed to provide space for the pressure tubing inside the model and the cockpit is closed in order to allow reliable mounting.

The model features a driver dummy, whose dimensions are set to a 95th percentile male in accordance with current Formula Student regulations.

To investigate the rear wing effectivity subject to varied inflow conditions, there are head restraints with constant width $b = 50$ mm but different heights installed downstream of the helmet. The studied configurations are introduced in Table 2. Note that configuration HR1, currently employed on the *FT17* original race car, represents the minimal head restraint size when a variable mounting height is allowed for, while HR3 constitutes the minimal size in the case of a non-variable mounting height. Configuration HR0 represents a scenario where the head restraint is removed but is not allowed by the current competition regulations for safety reasons.

Wind Tunnel Setup

The experiments are performed in a closed-loop wind tunnel with a maximum free-stream velocity of $U_{\infty,\,max} = 70\,\frac{m}{s}$ and a turbulence intensity of $Tu < 0.5\%$ inside the closed test section, which exhibits a cross section of $A = (2.00 \cdot 1.41)\,m^2$ [18]. This yields a blockage of $\varphi \approx 4.7\%$ in zero-yaw condition which is deemed acceptable by [19] - hence, no blockage correction is applied.

Unlike state of the art wind tunnels dedicated to vehicle aerodynamics [20], the facility does not provide a moving ground. Therefore, additional downforce generated by the
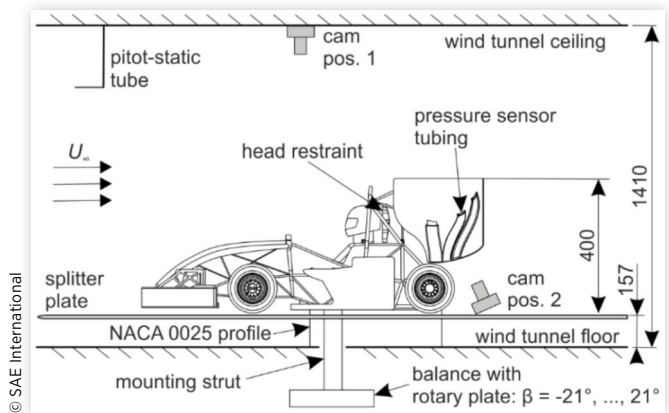
ground effect as explained in the introduction, is not reproduced. However, a splitter plate is present to separate the boundary layer entering the test section through the nozzle and boasting a thickness of $\delta_{99}/d_w \approx 1.2$ (normalized with wheel diameter) from the model underbody. Thus, a boundary layer of significantly lower thickness at the front wheels $\delta_{99}/d_w \approx 0.1$, emerging from the profiled leading edge of the splitter plate, interacts with the model.

As shown in Figure 2, the model is mounted on a six-component balance by means of a strut while ensuring a ground clearance of $\Delta z \approx 3$ mm in order to avoid traction. The strut reaches through the wind tunnel floor and the splitter plate and is shielded from the free-stream by a hollow NACA 0025 airfoil which allows to guide the pressure tubing outside the wind tunnel.
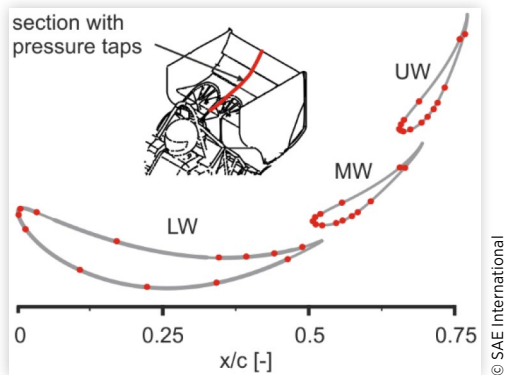
Photographs of the model inside the test section are provided in the appendix.

Measurement System and Method of Flow Visualization

To gain information regarding the aerodynamic forces acting on the model, the six-component lever balance, boasting an accuracy of 0.1% of measured value, is utilized. The balance exhibits a rotary plate, which is used to investigate yaw angles within the range of $\beta = -21, ..., 21°$. For the definition of the yaw angle, refer to Figure 1. Measurement samples are recorded over a time interval of $\Delta t = 15$ s and scanned at a frequency of $f = 1000$ Hz. However, only time-averaged data regarding the downforce (acting in negative z-direction), drag (x-direction) and side force (y-direction) are regarded in this study.

The wall pressure measurement on the rear wing is performed with the help of pressure taps inside three sections downstream of the head restraint with a spacing of $\Delta y/b \approx 0.32$, see Figure 3. Differential pressure sensors with an accuracy of 0.5% full scale and a range of $p_{max} = \pm 5{,}000$ Pa and $p_{max} = \pm 10{,}000$ Pa respectively are used, depending on the expected magnitude of differential pressure. The sampling rate is of the order of $f = 32{,}000$ Hz and the measurement

FIGURE 3 Location of pressure taps on three-element rear wing; c denotes the sum of chord lengths of wing elements.

© SAE International

FIGURE 4 Downforce as a function of yaw angle β for different aero package configurations.

© SAE International

duration is $\Delta t = 8$ s. Again, only time-averaged data is regarded. Therefore, tube length is uncritical and the sensors are placed outside the test section for better access. The reference pressure is gathered by the static port of the pitot-static tube upstream of the model, allowing for a computation of pressure coefficients $c_p(x) = \dfrac{p(x) - p_\infty}{q_\infty}$ at locations x shown in Figure 3.

In addition to the mentioned quantitative measurement techniques, flow visualization by means of UV active wool tufts is performed on the surface of the model for the configurations HR1 and HR4. While doing so, different colors of tufts are employed to better assign them to specific areas of the contour. The pictures are taken from the two positions depicted in Figure 2, using a reflex camera operated with a long-time exposure.

Results

In the following, the quantitative as well as qualitative results obtained by the techniques outlined in the previous section are presented. Thereby, the quality of the aero package of the investigated race car model and the influence of a varied head restraint size are determined.

Assessment of Aero Package Components

In order to evaluate the components of the aero package, force measurements of different configurations under varying crosswind conditions are conducted.

The induced downforce for a varied yaw angle β are shown in Figure 4. The baseline configuration, exhibiting no specific aerodynamic components, boasts an almost constant lift coefficient of $c_L \approx 0.15$ across all studied yaw angles. This is not only ascribed to a lack of downforce generating wings but also to the absence of a moving ground. Therefore, no significant downforce is produced by the underbody geometry through the ground effect outlined in the introduction of this article. Adding the front wing to the baseline configuration,
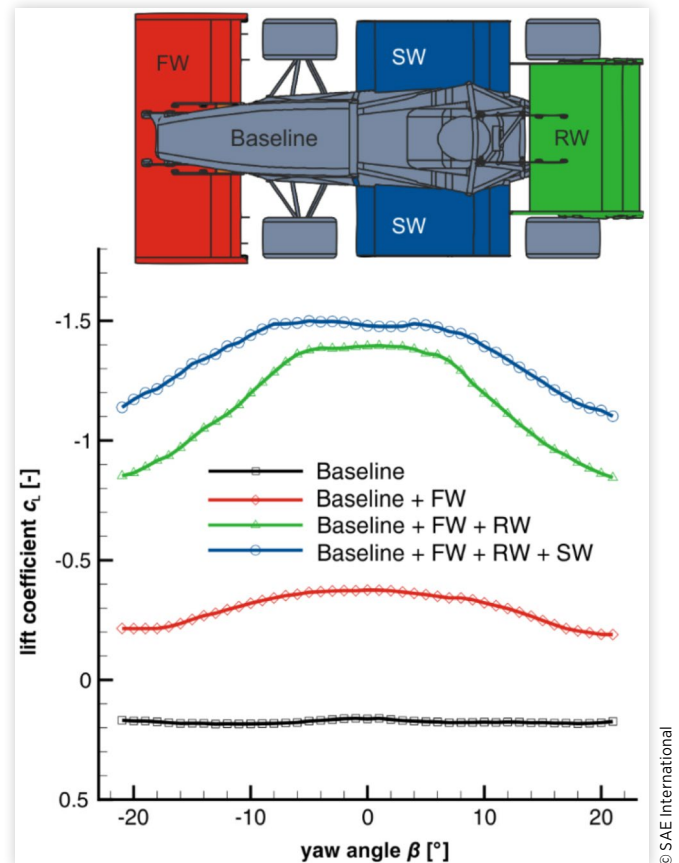
however, yields a downforce of the order of $c_L < -0.3$ at yaw angles of $|\beta| < 10°$, which are relevant to cornering maneuvers. The most significant improvement of downforce performance is achieved by the application of the three-element rear wing, increasing the downforce roughly by a factor of 4.

It can be noted that a relatively stable maximum in downforce of $c_L \approx -1.4$ is produced, spanning from $\beta = -5°$ to $\beta = 5°$ with a distinct decrease present beyond these yaw angles. This plateau is slightly lifted to values of $c_L \approx -1.5$ through the additional utilization of side wings. Additionally, the curve is flattened as maximum downforce is generated over a greater range of yaw angles. At this point, it should be noted that greater downforce contributions by the front wing, side wings and - to a lesser extent - the rear wing are expected under realistic conditions since these devices heavily exploit the ground effect as well.

The drag coefficient c_D subject to different configurations under varied yaw angles is depicted in Figure 5. The baseline configuration exhibits a drag coefficient of the order of $c_D \approx 0.42$ with a slight increase noticeable at non-neutral yaw angles. This can be explained by the drag inducing effect of vortex structures inside the near wake of the vehicle, which are generally more intense under crosswind conditions. The application of the front wing produces an increase in drag by about $\Delta c_D \approx 10\%$, which is balanced by the massive downforce enhancement outlined previously. The most distinct increase in aerodynamic drag, however, is produced by the addition of

FIGURE 5 Drag coefficient c_D as a function of yaw angle β for different aero package configurations.

FIGURE 6 Side force coefficient c_S as a function of yaw angle β for different aero package configurations.
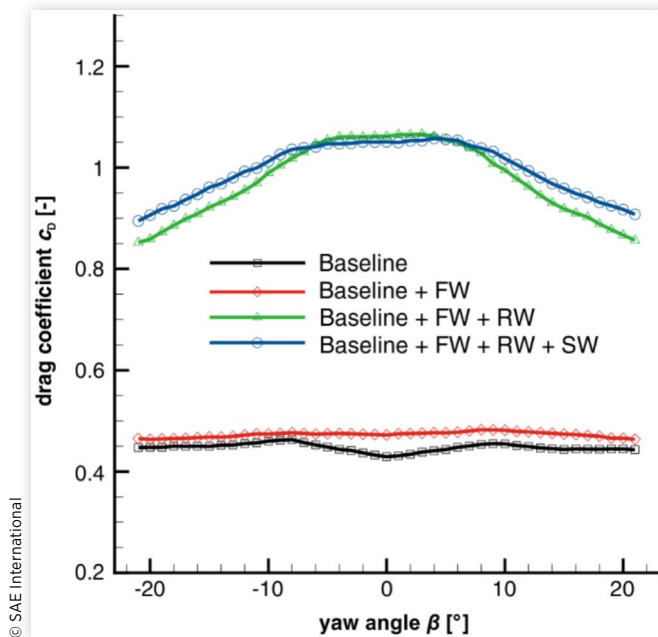
the rear wing, yielding coefficients of the order of $c_D > 1.0$ at small yaw angles. At greater angles, the drag coefficient is decreased, representing an inverted behavior when compared to the baseline configuration. This finding can be ascribed to the end plates partially blocking the flow toward the rear wing under crosswind conditions. Thus, the amount of fluid deflected by the rear wing is decreased, yielding smaller downforce and drag coefficients. The additional application of side wings further reduces the observed sensitivity regarding crosswind, increasing the drag coefficient only at yaw angles of $|\beta| > 7°$.

Figure 6 shows the side force coefficient c_S for the four aero package configurations. While a coefficient of $c_S \approx 0$ is found at $\beta = 0°$ in the case of all studied scenarios, the slopes of the curves vary. This is attributed to the rudder-type plates that border the front as well as the rear wing. Due to the greater size of the rear wing end plates, the side force is more significantly increased in magnitude at yaw angles of $\beta \neq 0°$ when the rear wing and the respective end plates are mounted to the model.

Influence of Head Restraint Size

In the following, the impact of the head restraint height is evaluated with respect to the flow toward the rear wing. At first, the flow state is investigated qualitatively by means of tuft visualization, uncovering turbulent regions of potential flow separation. Then, ensuing wall pressure distributions are presented and checked against the obtained force coefficients.

Qualitative Flow Visualization by means of UV Active Tufts
To visualize the flow along the race car model, UV active tufts are applied to its surface. Depending on the
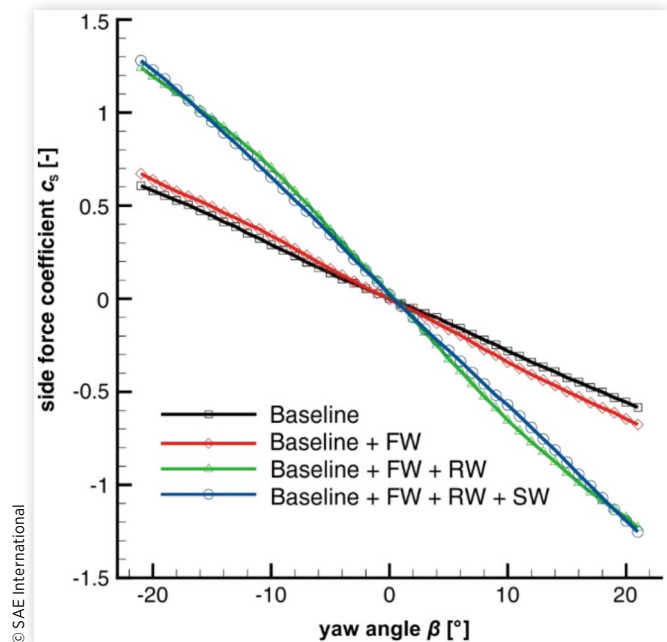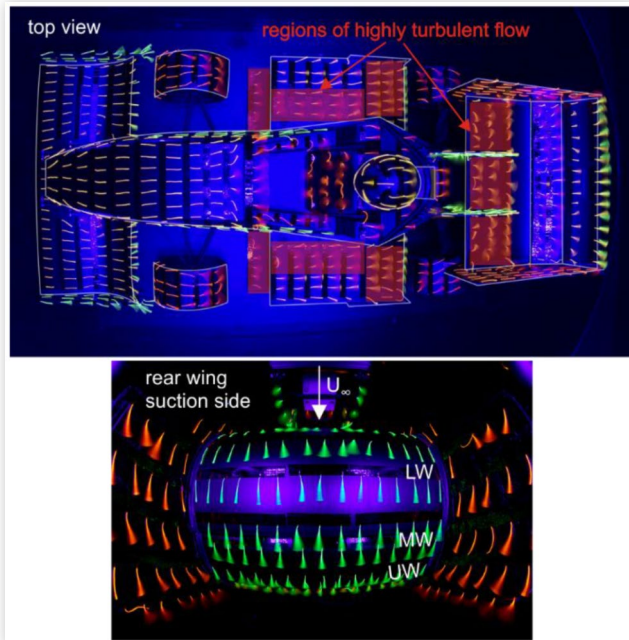
flow state, the tufts either exhibit a constant orientation (attached flow) or a variable deflection angle (increased turbulence intensity, potentially separated flow) when images with a sufficiently long exposure time are evaluated. Special focus is laid upon the flow condition inside the mid-section of the pressure and suction side of the rear wing as this area is influenced by the head restraint size. Therefore, images are taken from above the model and beneath the rear wing, denoted as positions 1 and 2 in Figure 2.

Figure 7 shows the results of the flow visualization for configuration HR2 at a yaw angle $\beta = 0°$. Regarding the aero package, it can be noted that the flow is generally attached with the exception of the leading edge and the inner sections of the side wings as well as the lower wing element of the rear wing. These regions are located inside the turbulent wakes of components that cause geometrically induced flow separation. Otherwise, an attached flow can be attested, enabling an effective downforce performance of the front wing, sections of the side wings and the middle and upper element of the rear wing.

In order to allow a comparison of tuft deflection angles between configuration HR2 and HR4, image subtraction is applied, involving corresponding pictures at different yaw angles, see Figure 8. Thus, regions of low color intensity indicate an unaltered flow scenario while visible tufts mark areas where the larger head restraint of configuration HR4 causes greater tuft deflection angles, i. e., more significant regions of flow separation.

Neglecting the driver body, whose nearly vertical orientation yields stochastic tuft deflections that are visible after image subtraction, the model contour of both configurations exhibits similar flow conditions with the exception of the rear wing. This finding is expected since merely the head restraint size is varied between the evaluated configurations, affecting only the flow toward the furthest downstream component of

FIGURE 7 Flow visualization of configuration HR2 at β = 0°; top view: regions of separated flow marked with red color; rear wing suction side: green tufts on wing elements and roll hoop, orange tufts on end plates, distorted view due to close camera proximity.

© SAE International

FIGURE 8 Top view of flow visualization: results of image subtraction of configurations HR2 and HR4 at β = [0, 5, 10]°.

© SAE International

the aero package. Therefore, the mid-section of the rear wing exhibits tufts that are visible after image subtraction. This is especially true for the lower and middle wing element where a decrease in downforce performance can be expected.

At the greatest displayed yaw angle of β = 10°, however, the difference between the studied configurations appears less distinct, spanning only the lower wing element of the rear wing.

The flow along the suction side of the rear wing is assessed in an analogous manner, see Figure 9. Regarding the neutral yaw angle β = 0°, it can be noted that the region of highly turbulent flow is enlarged by the greater head restraint of configuration HR4. This can be determined by the visible tufts at the leading edge of the lower wing element, on the upper wing and slightly outside the symmetry plane on the middle wing. By contrast, the outer sections of the rear wing as well as the inner sides of the end plates remain unaffected by the varied head restraint size. Generally, a drop in downforce regarding configuration HR4, can be expected due to a more distinct area of separated flow on the mid-section of the wing.

Under crosswind condition, the wake flow induced by the head restraint is slightly rotated. Thus, a displacement of the greatest tuft deflection angles toward one side can be observed. Again, the greater head restraint size appears to induce a larger region of separated flow, albeit to a lesser extent at β = 10°.

Rear Wing Wall Pressure Distributions As the surface pressure on the rear wing is measured downstream of the head restraint, the influence of its size can be quantitatively determined by means of the induced pressure distributions. Figure 10 shows the pressure coefficient c_p inside the symmetry plane as a function of the normalized x coordinate
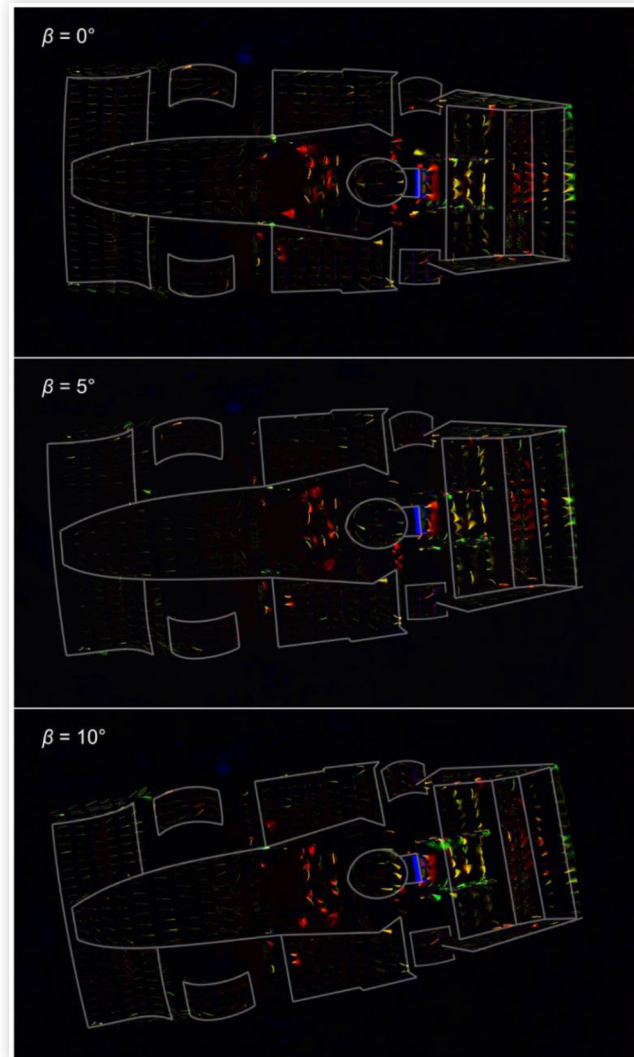
for the five investigated head restraint configurations at yaw angle β = 0°. Note that c equals the sum of chord lengths of the three rear wing elements.

When the suction side (LP) of the lower wing element is concerned, a trend is observable in that smaller head restraints produce a greater magnitude of the present pressure coefficient. This is especially true for the pressure taps located at $x/c \approx 0.1$ and $x/c \approx 0.2$ where values of $c_p \approx -0.6$ and $c_p \approx -0.9$ are produced in the case of configuration HR1 compared to $c_p \approx -0.4$ and $c_p \approx -0.75$ for the greatest investigated head restraint (HR4). This finding is in good agreement with the previously presented results of the performed flow visualization. The pressure side (HP) of the lower wing exhibits similar distributions for the head restraints of different size with the exception of configuration HR4 again generating pressure coefficients of smaller magnitude. However, it can be noted that a head restraint, even of minimum size, positively affects the pressure distribution as there are distinctly small pressure coefficients noticeable at x/c < 0.2 in the case of no head restraint (HR0).

FIGURE 9 Bottom view of flow visualization on rear wing: results of image subtraction of configurations HR2 and HR4 at $\beta = [0, 5, 10]°$.

© SAE International
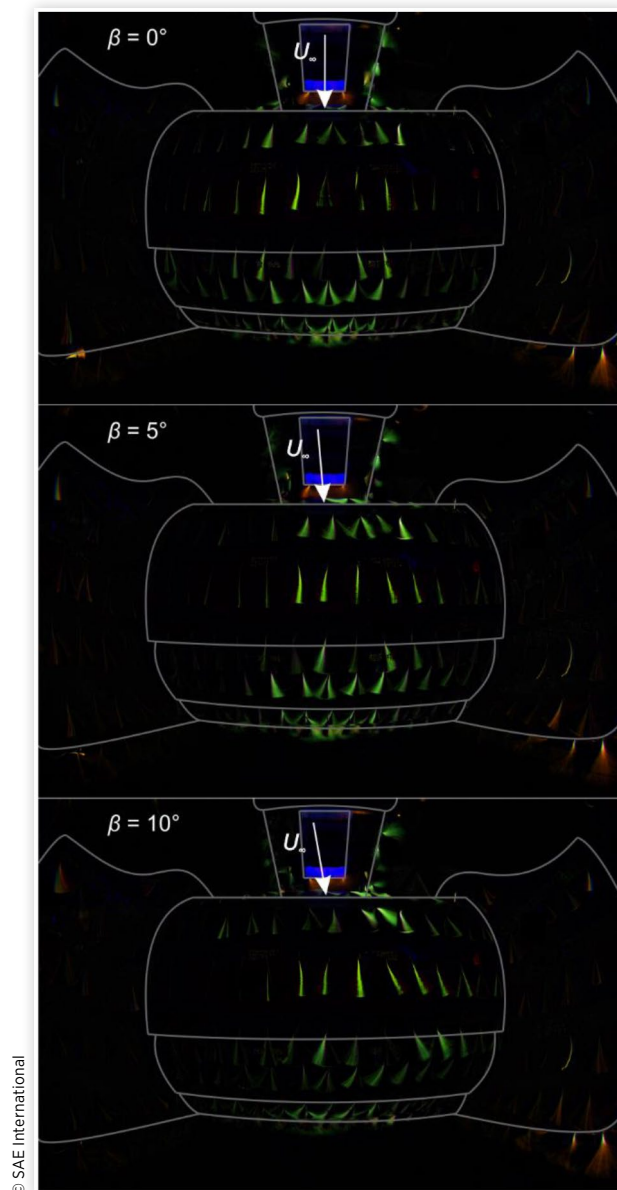
The same is not applicable to the pressure sides of the middle wing and the upper wing respectively where the pressure distributions of configurations HR0 through HR3 are nearly identical. The greater pressure level concerning these elements can be ascribed to the greater degree of flow deflection and less pronounced regions of highly turbulent flow as shown through flow visualization in the previous subsection. Maximum pressure coefficients of $c_p \approx 0.7$ are achieved on both of the smaller rear wing elements close to the leading edge in contrast to $c_p \approx 0.55$ (MW) and $c_p \approx 0.6$ (UW) for the largest head restraint (HR4). The suction sides yield minimum pressure coefficients of the order of $c_p \approx -1.5$ for configurations HR0 through HR3 and $c_p \approx -1.3$ for configuration HR4.

From analyzing the pressure distributions inside the symmetry plane at $\beta = 0°$, it can be generally assumed that the

head restraint size predominantly affects the suction side of the lower wing element as long as a threshold regarding the height is not exceeded.

Figure 11 illustrates the downforce generated by the individual rear wing elements at different yaw angles inside the symmetry plane of the wing, i. e., the section enclosed by pressure taps. Note that a linear numerical integration scheme is applied to compute the displayed lift coefficients.

Despite the greater chord length of the lower wing, the downforce contribution is not significantly larger than for the other rear wing elements. This can be attributed to the generally smaller pressure magnitude shown in Figure 10.

With regards to the neutral yaw angle $\beta = 0°$, the previously presented results can be confirmed. The configurations HR0 through HR3 yield a similar downforce performance of the order of $c_l \approx -0.88$ while a performance decrease by $\Delta c_l \approx 16\%$ is observed in the case of the largest head restraint.

At a yaw angle of $\beta = 5°$, however, the level of downforce decreases slightly in the case of the smaller head restraint whereas it increases for configuration HR4. Apparently, the height of the head restraint becomes less significant under slight crosswind conditions.
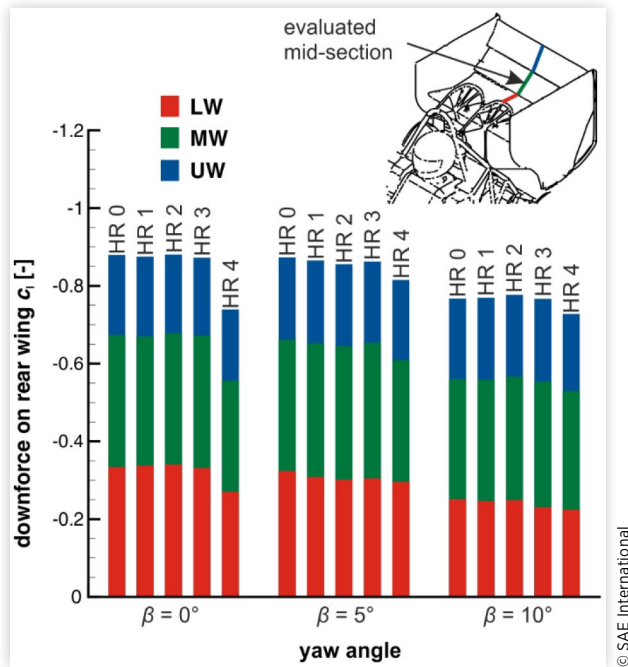
For the greatest displayed yaw angle $\beta = 10°$, the level of downforce is relatively even with configuration HR4 only

FIGURE 10 Wall pressure distributions in symmetry plane on rear wing elements subject to varied head restraint size; yaw angle set to $\beta = 0°$.

© SAE International
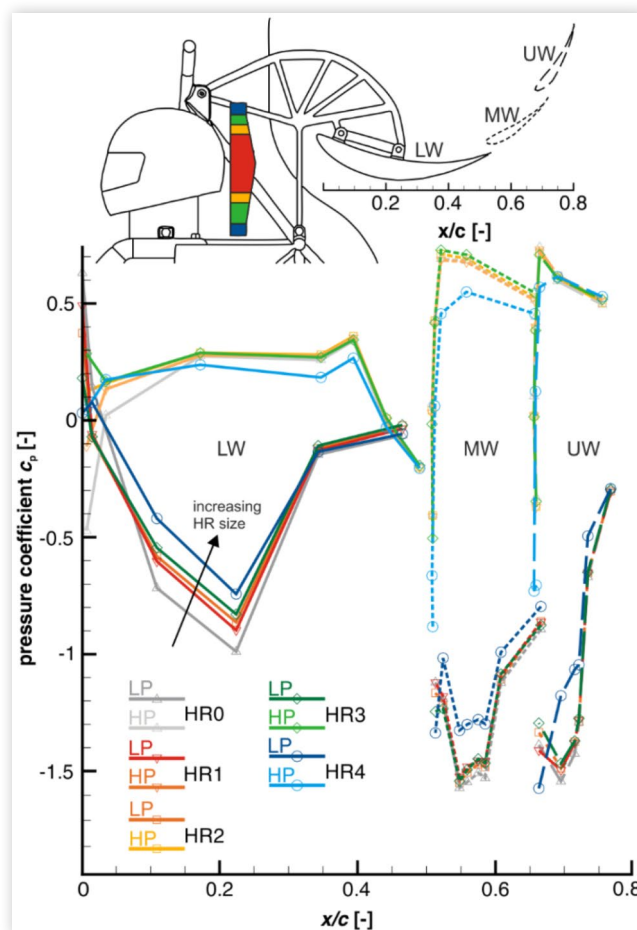
FIGURE 11 Downforce acting on mid-section of rear wing; contribution of individual elements.

© SAE International

FIGURE 12 Load proportion on rear axle for different Reynolds numbers.

© SAE International

slightly falling away at $c_l \approx -0.73$ compared to $c_l \approx -0.77$ in the case of the other configurations.

Shift of Axle Loading As lined out above, changing the head restraint size primarily affects the rear wing efficiency. Therefore, the proportion of load acting on the rear axle is affected, having slight implications in terms of the drivability. This issue is addressed in Figure 12, where the load proportion on the rear axle is shown for relevant Reynolds numbers. Note that the weight force of race car plus driver F_G is considered as well.

Due to the center of gravity being slightly closer to the front axle, the load proportion is shifted toward the front at low Reynolds numbers. At greater driving speed, the downforce acting on the rear wing increases and causes a shift of the total load toward the rear axle. It can be observed that configuration HR4 yields a slight decrease of rear axle loading by approximately 1% due to the smaller pressure magnitude discussed above. Thus, a level load distribution is only achieved at a Reynolds number of $Re \approx 7.6 \cdot 10^5$ compared to $Re \approx 5.3 \cdot 10^5$ for the other configurations.

Induced Total Downforce and Drag In this subsection, results regarding the total downforce and drag acting on the model at different head restraint configurations are presented.

Figure 13 displays the downforce subject to a variation of the yaw angle. Generally, it can be noted that configuration HR4, representing the largest head restraint, is associated with significantly less downforce compared to the other configurations. A decrease of the head restraint height by $\Delta h \approx 20$ mm from HR4 to HR3 yields an increase in downforce by $\Delta c_L \approx 5.5\%$ at $\beta = 0°$. Further decreasing the head restraint
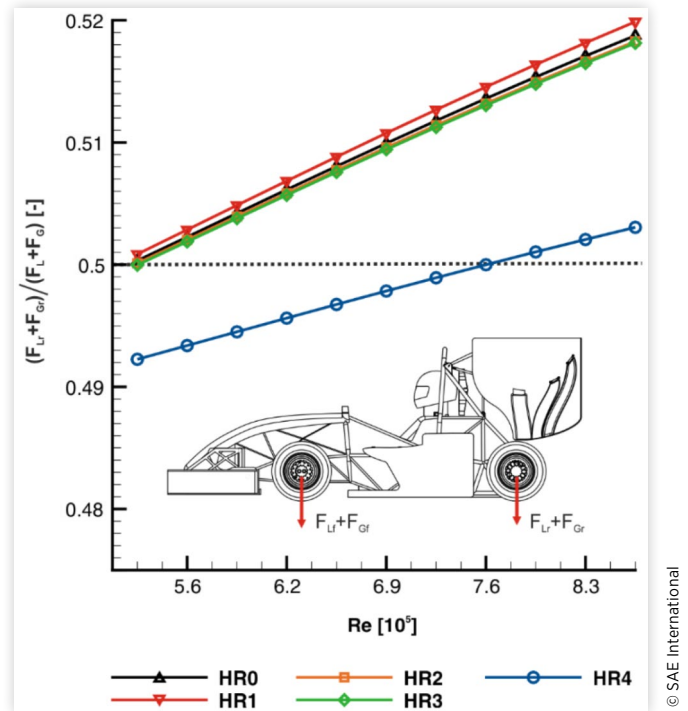
FIGURE 13 Downforce coefficient subject to varied head restraint size.


© SAE International
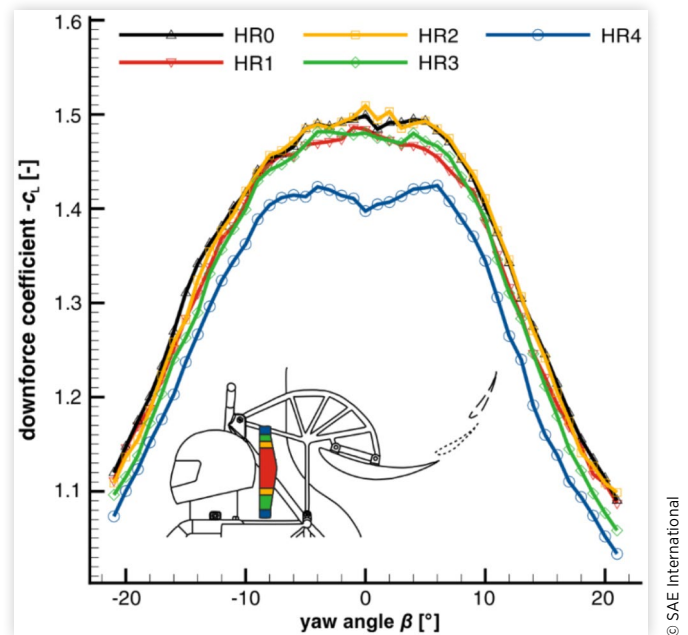
height does not cause as significant margins in downforce. It can even be found that configuration HR2 yields a slightly superior performance compared to the baseline head restraint represented by configuration HR1.

While configurations HR0 through HR3 generally exhibit a downforce maximum at $\beta = 0°$ as well as a stable high level

FIGURE 14 Drag coefficient subject to varied head restraint size.
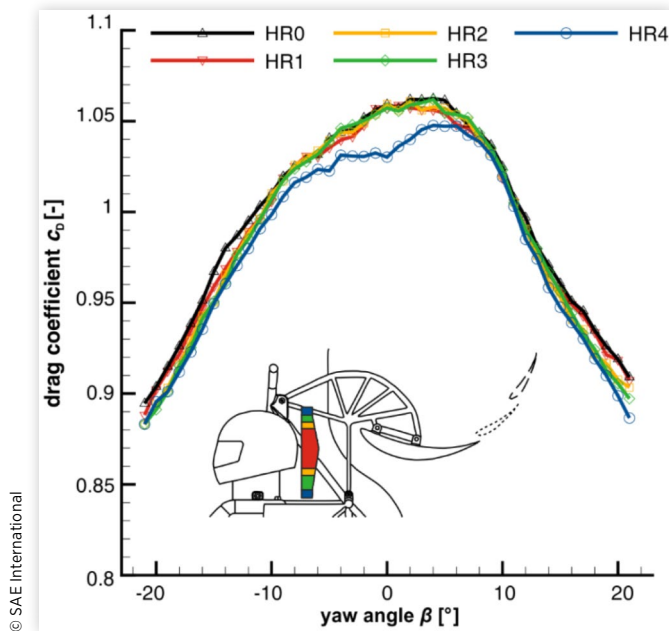
of downforce up to $|\beta| = 6°$ and a subsequent rapid decrease, the largest investigated head restraint produces a maximum in downforce at $|\beta| \approx 6°$. This finding is in agreement with the bar chart in Figure 11, indicating that slight crosswind conditions improve the aerodynamic characteristics of configuration HR4 with respect to downforce.

The drag force induced by the various head restraint configurations is illustrated in Figure 14. Slightly asymmetric curves are noticeable with drag maxima of all configurations being present at $\beta \approx 4°$, which may be attributed to production imperfections.

While the smaller head restraints induce similar drag coefficients across the studied yaw angles, the largest head restraint partially blocks the flow toward the rear wing. Thus, slightly smaller drag coefficients are achieved - especially in the case of small yaw angles. However, this benefit is more than offset by the significantly smaller downforce generated.

Conclusions

The aim of the present article is to investigate the aerodynamic components of a realistic open-wheel race car and evaluate the influence of the head restraint height with respect to downforce performance. For this purpose, qualitative as well as quantitative experimental methods are employed. The measurement procedure involves a variation of the yaw angle within the range of $\beta = -21, …, 21°$ for five configurations HR0 through HR4, representing head restraint heights of the order of $h = [0.0; 50.0; 66.5; 93.0; 113.3]$ mm.

With regards to the aero package components, the downforce is significantly increased by the front as well as the rear wing, producing downforce coefficients of the order of $c_L \approx -0.35$ (front wing only) and $c_L \approx -1.4$ (front wing and

rear wing installed) at a neutral yaw angle. The additional application of side wings further increases the induced downforce while stabilizing the maximum of $c_L \approx -1.5$ with respect to crosswind conditions across a range of $\beta = -7, …, 7°$, which is relevant to most cornering maneuvers.

By means of flow visualization experiments using UV active tufts, the surface flow along the race car model is studied. Thereby, large sections of highly turbulent and potentially separated flow on the side wings and on the rear wing are identified. When comparing the influence of the largest studied head restraint (HR4) to the device currently employed on the original race car (HR1), an enlargement of these regions on both the pressure and the suction side of the three-element rear wing is observed. This particularly applies to the lower wing element.

The latter finding is confirmed through surface pressure measurement in three longitudinal sections along the rear wing. Regarding the suction side of the lower wing element, it can be noted that a decrease in head restraint size generally yields an increase in pressure magnitude. On the other wing elements, however, similar pressure distributions are observed with the exception of configuration HR4 exhibiting consistently smaller pressure magnitudes. This can be explained by the fact that an optimal guidance of flow along the lower wing is prerequisite in ensuring the efficiency of the middle and upper wing.

Consequently, force measurements of the different configurations show similar characteristics for the configurations HR0 through HR3. However, the larger head restraint represented by configurations HR2 yields a slightly improved aerodynamic performance compared to the baseline configuration HR1. In line with safety precautions, a minor enlargement of the head restraint can therefore be recommended. However, beyond a certain threshold, a distinctly negative effect is detected with the downforce at $\beta = 0°$ being reduced by $\Delta c_L \approx 5.5\%$ (HR4). Taking into account the great significance of downforce generated by modern race cars, this represents a major performance gap.

References

1. Katz, J., "Aerodynamics of Race Cars," *Annual Review of Fluid Mechanics* 38:27-63, 2006, doi:10.1146/annurev. fluid.38.050304.092016.

2. Johansson, M.O. and Katz, J., "Lateral Aerodynamics of a Generic Sprint Car Configuration," SAE Technical Paper 2002-01-3312, 2002, doi:10.4271/2002-01-3312.

3. Jasinski, W.J. and Selig, M.S., "Experimental Study of Open-Wheel Race-Car Front Wings," SAE Technical Paper 983042, 1998, doi:10.4271/983042.

4. Dominy, R.G., "Aerodynamics of Grand Prix Cars," *Proceedings of the Instution of Mechanical Engineers* 206(44):267-274, 1992, doi:10.1243/PIME_PROC_1992_206_187_02.

5. Devaiah, B.N. and Umesh, S., "Enhancement of Aerodynamic Performance of a Formula-1 Race Car Using Add-on Devices," *SASTech Journal* 12(1):72-79, 2013.

6. Hammond, A. R. and Flay, R. G. J., "*Aerodynamic Design of a Formula SAE Race Car*," BBAA VI International Colloquium on: Bluff Bodies Aerodynamics & Applications, 2008

7. Katz, J. and Garcia, D., "Aerodynamic Effects of Indy Car Components," SAE Technical Paper 2002-01-3311, 2002, doi:10.4271/2002-01-3311.

8. Kajiwara, S., "Passive Variable Rear-Wing Aerodynamics of an Open-Wheel Racing Car," *Automotive and Engine Technology*, 2017, doi:10.1007/s41104-017-0021-9.

9. Djavareshkian, M.H. and Esmaeli, A., "Smart Spoiler for Race Car," *International Journal of Mechanical, Aeronautical, Industry, Mechatronics Manufacture Engineering* 5(1):97-103, 2011.

10. Kieffer, W., Moujaes, S., and Armbya, N., "CFD Study of Section Characteristics of Formula Mazda Race Car Wings," *Mathematical and Computer Modelling* 43(11-12):1275-1287, 2006, doi:10.1016/j.mcm.2005.03.011.

11. Mokhtar, W. and Durrer, S., "A CFD Analysis of a Racer Car Front Wing in Ground Effect," *Proceedings ASEE North Central Section Conference*, 2016.

12. Zerihan, J. and Zhang, X., "Aerodynamics of a Single Element Wing in Ground Effect," *Journal of Aircraft* 37(6):1058-1064, 2000, doi:10.2514/2.2711.

13. Soso, M.D. and Wilson, P.A., "Aerodynamics of a Wing in Ground Effect in Generic Racing Car Wake Flows," *Proceedings of the Institution of Mechanical Engineers, Part D: Journal of Automobile Engineering* 220, 2006, doi:10.1243/095440705X69632.

14. Dominy, R.G., "The Influence of Slipstreaming on the Performance of a Grand Prix Racing Car," *Proceedings of Instution of Mechanical Engineers* 204(14):35-40, 1990, doi:10.1243/PIME_PROC_1990_204_130_02.

15. Senior, A.E. and Zhan, X., "The Force and Pressure of a Diffuser-Equipped Bluff Body in Ground Effect," *Journal of Fluids Engineering* 123(1):105-111, 2001, doi:10.1115/1.1340637.

16. Garcia, D.L. and Katz, J., "Trapped Vortex in Ground Effect," *AIAA Journal* 41(4):674-678, 2005, doi:10.2514/2.1997.

17. Venkatesan, D.V., Shanjay, K.E., Sujith, K.H., Abhilash, N.A. et al., "Studies on Race Car Aerodynamics at Wing in Ground Effect," *International Journal of Mechanical, and Mechatronic Engineering* 8(7):1169-1174, 2014.

18. Technische Universität Berlin, FG Experimentelle Strömungsmechanik, "*Großer Windkanal (GroWiKa)*" technical description, 2017 http://fd.tu-berlin.de/einrichtungen/windkanaele/growika/.

19. Hucho, W.-H., editor, "*Aerodynamik des Automobils*," 6th Edition (Springer Vieweg, 2013), doi:10.1007/978-3-8348-2316-8.

20. le Good, G. M., Passmore, M. A., Cogotti, A., "A Comparison of On-Road Aerodynamic Drag Measurements with Wind Tunnel Data from Pininfarina and MIRA," SAE Technical Paper 980394, 1998, doi:10.4271/980394.

## Acknowledgments

Definitions/Abbreviations

FW - front wing

HP - pressure side of rear wing

HR - head restraint

LP - suction side of rear wing

LW - lower wing element of rear wing

MW - middle wing element of rear wing

RW - rear wing

SW - side wing

UV - ultraviolet

UW - upper wing element of rear wing

Contact Information

frank.haucke.1@tu-berlin.de
ben.steinfurth@tu-berlin.de
TU Berlin, ILR, Sekr. F2
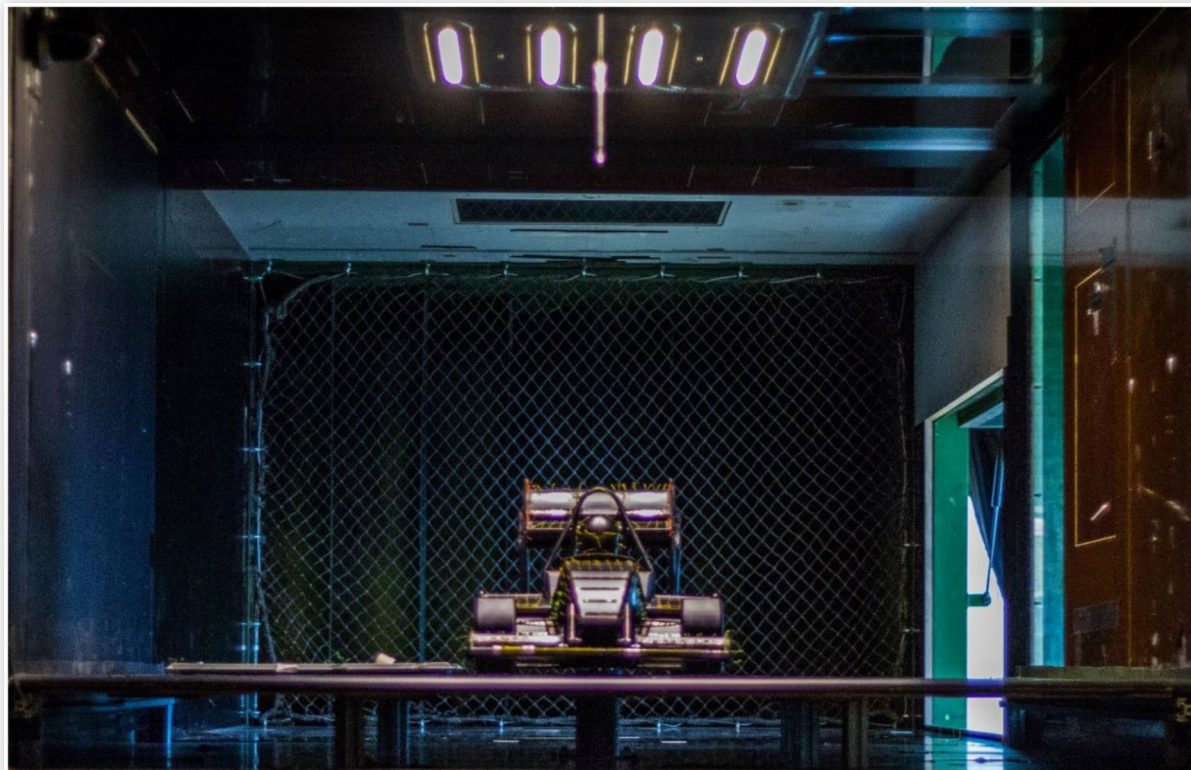Marchstraße 12-14, 10587 Berlin
Germany

Appendix: Pictures of Investigated Model

FIGURE A1   Model with UV active tufts inside test section on rotary plate.
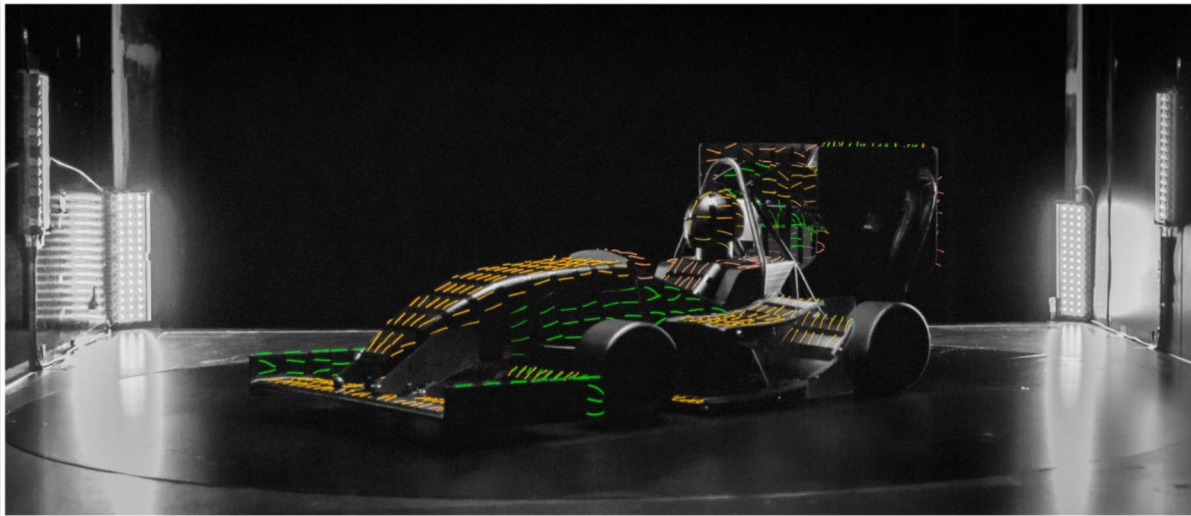
© SAE International

FIGURE A2   Model inside test section during preparation for wind tunnel tests; viewpoint upstream of nozzle, inside the settling chamber.

© SAE International